Simply, linear correction could be applied to convert to the apparent k value as has been performed in this study. $CMRO_2$ values calculated using BM approach for the RW separation, were in good agreement with those determined with the direct measurement of RW as shown in Table 3.

The current method with modeling approach and simplified procedure provided consistent results in terms of time-dependent RW component, and consequently metabolic product of $^{15}O_2$ was separated from arterial whole blood for the $CMRO_2$ assessment in PET examination. The modeling approach to separate metabolite from authentic tracer has been showed previously for 6-[^{18}F]fluoro-L-dopa study (fdopa) (Huang et al, 1991). We expect that the modeling approach in conjunction with the simplified method showed in our study could be applied for various kinds of tracers, which require the separation of metabolic product such as fdopa. This approach enables us to assess parametric images for those tracers by eliminating the laborious procedures and by avoiding the amount of blood samplings, particularly for smaller animals.

In conclusion, the present RW model was feasible to reproduce RW TAC from a whole radioactivity concentration curve obtained after $^{15}O_2$ inhalation, and for a wide range of species. The simplified procedure to predict the RW TAC is of use to calculate $CMRO_2$ in smaller animals as well as clinical patients.

Acknowledgements

References

Aston JA, Cunningham VJ, Asselin MC, Hammers A, Evans AC, Gunn RN (2002) Positron emission tomography partial volume correction: estimation and algorithms. *J Cereb Blood Flow Metab* 22:1019–34

Eriksson L, Holte S, Bohm Chr, Kesselberg M, Hovander B (1988) Automated blood sampling system for positron emission tomography. *IEEE Trans Nucl Sci* 35:703–7

Eriksson L, Kanno I (1991) Blood sampling devices and measurements. *Med Prog Technol* 17:249–57

Fujita H, Kuwabara H, Reutens DC, Gjedde A (1999) Oxygen consumption of cerebral cortex fails to increase during continued vibrotactile stimulation. *J Cereb Blood Flow Metab* 19:266–71

Hayashi T, Watabe H, Kudomi N, Kim KM, Enmi J, Hayashida K, Iida H (2003) A theoretical model of oxygen delivery and metabolism for physiologic interpretation of quantitative cerebral blood flow and metabolic rate of oxygen. *J Cereb Blood Flow Metab* 23:1314–23

Hirano T, Minematsu K, Hasegawa Y, Tanaka Y, Hayashida K, Yamaguchi T (1994) Acetazolamide reactivity on ^{123}I-IMP single photon emission computed tomography in patients with major cerebral artery occlusive disease: correlation with positron emission tomography parameters. *J Cereb Blood Flow Metab* 14:763–70

Holden JE, Eriksson L, Roland PE, Stone-Elander S, Widen L, Kesselberg M (1988) Direct comparison of single-scan autoradiographic with multiple-scan least-squares fitting approaches to PET $CMRO_2$ estimation. *J Cereb Blood Flow Metab* 8:671–80

Huang SC, Barrio JR, Yu DC, Chen B, Grafton S, Melega WP, Hoffman JM, Satyamurthy N, Mazziotta JC, Phelps ME (1991) Modelling approach for separating blood time-activity curves in positron emission tomographic studies. *Phys Med Biol* 36:749–61

Iida H, Jones T, Miura S (1993) Modeling approach to eliminate the need to separate arterial plasma in oxygen-15 inhalation positron emission tomography. *J Nucl Med* 34:1333–40

Iida H, Kanno I, Miura S, Murakami M, Takahashi K, Uemura K (1989) A determination of the regional brain/blood partition coefficient of water using dynamic positron emission tomography. *J Cereb Blood Flow Metab* 9:874–85

Kaisti KK, Langsjo JW, Aalto S, Oikonen V, Sipila H, Teras M, Hinkka S, Metsahonkala L, Scheinin H (2003) Effects of sevoflurane, propofol, and adjunct nitrous oxide on regional cerebral blood flow, oxygen consumption, and blood volume in humans. *Anesthesiology* 99:603–13

Kudomi N, Choi C, Watabe H, Kim KM, Shidahara M, Ogawa M, Teramoto N, Sakamoto E, Iida H (2003) Development of a GSO detector assembly for a continuous blood sampling system. *IEEE Trans Nucl Sci* 50:70–3

Kudomi N, Hayashi T, Teramoto N, Watabe H, Kawachi N, Ohta Y, Kim KM, Iida H (2005) Rapid quantitative measurement of $CMRO_2$ and CBF by dual administration of ^{15}O-labeled oxygen and water during a single PET scan—a validation study and error analysis in anesthetized monkeys. *J Cereb Blood Flow Metab* 25:1209–24

Kudomi N, Watabe H, Hayashi T, Iida H (2007) Separation of input function for rapid measurement of quantitative $CMRO_2$ and CBF in a single PET scan with a dual tracer administration method. *Phys Med Biol* 52:1893–908

Laforest R, Sharp TL, Engelbach JA, Fettig NM, Herrero P, Kim J, Lewis JS, Rowland DJ, Tai YC, Welch MJ (2005) Measurement of input functions in rodents: challenges and solutions. *Nucl Med Biol* 32:679–85

Lindstedt L, Schaeffer PJ (2002) Use of allometry in predicting anatomical and physiological parameters of mammals. *Lab Anim* 36:1–19

Magata Y, Temma T, Iida H, Ogawa M, Mukai T, Iida Y, Morimoto T, Konishi J, Saji H (2003) Development of injectable O-15 oxygen and estimation of rat OEF. *J Cereb Blood Flow Metab* 23:671–6

Meyer E, Tyler JL, Thompson CJ, Redies C, Diksic M, Hakim AM (1987) Estimation of cerebral oxygen utilization rate by single-bolus 15O2 inhalation and dynamic positron emission tomography. *J Cereb Blood Flow Metab* 7:403–14

Mintun MA, Raichle ME, Martin WR, Herscovitch P (1984) Brain oxygen utilization measured with O-15 radio-

tracers and positron emission tomography. *J Nucl Med* 25:177–87

Mintun MA, Vlassenko AG, Shulman GL, Snyder AZ (2002) Time-related increase of oxygen utilization in continuously activated human visual cortex. *Neuroimage* 16:531–7

Ohta S, Meyer E, Thompson CJ, Gjedde A (1992) Oxygen consumption of the living human brain measured after a single inhalation of positron emitting oxygen. *J Cereb Blood Flow Metab* 12:179–92

Okazawa H, Yamauchi H, Sugimoto K, Takahashi M, Toyoda H, Kishibe Y, Shio H (2001a) Quantitative comparison of the bolus and steady-state methods for measurement of cerebral perfusion and oxygen metabolism: positron emission tomography study using 15O-gas and water. *J Cereb Blood Flow Metab* 21:793–803

Okazawa H, Yamauchi H, Sugimoto K, Toyoda H, Kishibe Y, Takahashi M (2001b) Effects of acetazolamide on cerebral blood flow, blood volume, and oxygen metabolism: a positron emission tomography study with healthy volunteers. *J Cereb Blood Flow Metab* 21:1472–9

Pain F, Laniece P, Mastrippolito R, Gervais P, Hantraye P, Besret L (2004) Arterial input function measurement without blood sampling using a beta-microprobe in rats. *J Nucl Med* 45:1577–82

Sakoh M, Gjedde A (2003) Neuroprotection in hypothermia linked to redistribution of oxygen in brain. *Am J Physiol Heart Circ Physiol* 285:H17–25

Shidahara M, Watabe H, Kim KM, Oka H, Sago M, Hayashi T, Miyake Y, Ishida Y, Hayashida K, Nakamura T, Iida H (2002) Evaluation of a commercial PET tomograph-based system for the quantitative assessment of rCBF, rOEF and rCMRO2 by using sequential administration of 15O-labeled compounds. *Ann Nucl Med* 16:317–27

Temma T, Magata Y, Kuge Y, Shimonaka S, Sano K, Katada Y, Kawashima H, Mukai T, Watabe H, Iida H, Saji H (2006) Estimation of oxygen metabolism in a rat model of permanent ischemia using positron emission tomography with injectable^{15}O-O$_2$. *J Cereb Blood Flow Metab* 26:1577–83

Vafaee MS, Gjedde A (2000) Model of blood-brain transfer of oxygen explains nonlinear flow-metabolism coupling during stimulation of visual cortex. *J Cereb Blood Flow Metab* 20:747–54

Votaw JR, Shulman SD (1998) Performance evaluation of the Pico-Count flow-through detector for use in cerebral blood flow PET studies. *J Nucl Med* 39:509–15

Weber B, Burger C, Biro P, Buck A (2002) A femoral arteriovenous shunt facilitates arterial whole blood sampling in animals. *Eur J Nucl Med Mol Imaging* 29:319–23

Wessen A, Widman M, Andersson J, Hartvig P, Valind S, Hetta J, Langstrom B (1997) A positron emission tomography study of cerebral blood flow and oxygen metabolism in healthy male volunteers anaesthetized with eltanolone. *Acta Anaesthesiol Scand* 41:1204–12

Yamauchi H, Okazawa H, Kishibe Y, Sugimoto K, Takahashi M (2003) The effect of acetazolamide on the changes of cerebral blood flow and oxygen metabolism during visual stimulation. *Neuroimage* 20:543–9

Yee SH, Lee K, Jerabek PA, Fox PT (2006) Quantitative measurement of oxygen metabolic rate in the rat brain using microPET imaging of briefly inhaled 15O-labelled oxygen gas. *Nucl Med Commun* 27:573–81

Slowly progressive neuronal death associated with postischemic hyperperfusion in cortical laminar necrosis after high-flow bypass for a carotid intracavernous aneurysm

Case report

Koji Iihara, M.D., Ph.D., Masakazu Okawa, M.D., Tomohito Hishikawa, M.D., Ph.D., Naoaki Yamada, M.D., Ph.D., Kazuhito Fukushima, M.D., Ph.D., Hidehiro Iida, Ph.D., and Susumu Miyamoto, M.D., Ph.D.

Departments of Neurosurgery and Radiology, National Cardiovascular Center, Osaka, Japan

The authors report a rare case of slowly progressive neuronal death associated with postischemic hyperperfusion in cortical laminar necrosis after radial artery/external carotid artery–middle cerebral artery bypass graft surgery for an intracavernous carotid artery aneurysm. Under barbiturate protection, a 69-year-old man underwent high-flow bypass surgery combined with carotid artery sacrifice for a symptomatic intracavernous aneurysm. The patient became restless postoperatively, and this restlessness peaked on postoperative Day (POD) 7. Diffusion-weighted and FLAIR MR images obtained on PODs 1 and 7 revealed subtle cortical hyperintensity in the temporal cortex subjected to temporary occlusion. On POD 13, ^{123}I-iomazenil (^{123}I-IMZ) SPECT clearly showed increased distribution on the early image and mildly decreased binding on the delayed image with count ratios of the affected–unaffected corresponding regions of interest of 1.23 and 0.84, respectively, suggesting postischemic hyperperfusion. This was consistent with the finding on ^{123}I-iodoamphetamine SPECT. Of note, neuronal density in the affected cortex on the delayed ^{123}I-IMZ image further decreased to the affected/unaffected ratio of 0.44 on POD 55 during the subacute stage when characteristic cortical hyperintensity on T1-weighted MR imaging, typical of cortical laminar necrosis, was emerging. The affected cortex showed marked atrophy 8 months after the operation despite complete neurological recovery. This report illustrates, for the first time, dynamic neuroradiological correlations between slowly progressive neuronal death shown by ^{123}I-IMZ SPECT and cortical laminar necrosis on MR imaging in human stroke. (DOI: 10.3171/2009.9.JNS09345)

KEY WORDS • laminar necrosis • iomazenil • bypass • delayed neuronal death • magnetic resonance imaging

CORTICAL laminar necrosis is a permanent brain injury radiologically characterized by T1-weighted MR imaging–documented high-intensity cortical lesions that follow the gyral anatomy of the cerebral cortex.[7,17,19] It has been associated with hypoxia, metabolic disturbances, drugs, infections, status epilepticus, and ischemic stroke.[7,19] The neuropathological correlations, however, between neuronal loss and an emerging cortical T1 hyperintensity signal in human stroke remain unknown. Intracavernous CA aneurysms are usually treated by trapping with/without EC-IC bypass based on presumed tolerance to CA sacrifice.[6,9] Flumazenil and iomazenil are markers of central benzodiazepine receptors, part of the GABAergic complex,[2] and are ideal markers

of periinfarct tissue and incomplete brain infarcts.[16] This is the first report illustrating slowly progressive neuronal death, shown by ^{123}I-IMZ, during emerging cortical laminar necrosis on MR imaging after temporary occlusion at high-flow bypass for an intracavernous CA aneurysm.

Case Report

History and Examination. This 69-year-old man developed double vision and ptosis due to left oculomotor palsy. Angiograms obtained at the previous hospital showed bilateral large intracavernous CA aneurysms (Fig. 1A). After balloon test occlusion showing intolerance on temporary occlusion of the left CA, the patient was referred to our institution.

Operation. The patient's left large CA aneurysm was trapped by RA/ECA-MCA bypass grafting without causing any neurological deficit. Temporary occlusion of the inferior trunk of M_2 was performed for 52 minutes under thiopental brain protection. Postoperative MR dif-

fusion weighted imaging demonstrated no abnormality. Two months later, the patient presented with contralateral oculomotor palsy due to progressive growth of the contralateral aneurysm. He underwent virtually the same operation, except with a shorter duration of temporary occlusion (47 minutes) and except for the observation that back flow from the distal M_2 was slower and dark when the distal clip was first declamped after anastomosis, suggesting that the territory of the recipient artery had been subjected to ischemic insult due to insufficient collateral flow.

Postoperative Course. The patient awoke from anesthesia relatively soon without apparent neurological deficit. Diffusion weighted and FLAIR imaging on POD 1 showed slight cortical hyperintensity in the right temporal region (Fig. 1C and D). Angiograms obtained on POD 5 showed no opacification of the aneurysm and good bypass patency, but the patient gradually became restless. Diffusion weighted and FLAIR imaging repeated on POD 7 revealed similar findings (Fig. 1E and F). Because the signal change on diffusion weighted imaging, however, remained subtle, the cause of such MR imaging abnormality remained uncertain. Subtle Gd enhancement was noted in the temporal cortex. On POD 18, ^{123}I-IMZ SPECT showed increased distribution on the early image (15 minutes) and decreased binding on the delayed image (3 hours) in the temporal region corresponding to the hyperintensity area on diffusion weighted and FLAIR images (Fig. 2). Because early and delayed images of ^{123}I-IMZ SPECT represent the cerebral perfusion state and neuronal viability, respectively, these results clearly indicated that ischemic neuronal loss and postischemic hyperperfusion occurred as a result of ischemic insult by temporary occlusion during bypass surgery.

Chronological count ratio changes of the affected to the unaffected corresponding regions of interest on ^{123}I-IMZ and ^{123}I-IMP SPECT scans are shown in Fig. 3. In the temporal region subjected to temporary clipping, the affected/unaffected ratio on ^{123}I-IMZ scans decreased during the subacute period between PODs 18 (ratio 0.84) and 55 (ratio 0.44), and then it leveled off later (ratio 0.43 on POD 239), whereas it remained relatively constant in other regions. We did not obtain ^{123}I-IMZ SPECT scans before the operation. On ^{123}I-IMP SPECT, the affected/unaffected ratio transiently increased during PODs 13 (ratio 1.21) and 26 (ratio 1.23), and it progressively decreased on PODs 53 (ratio 0.84) and 236 (ratio 0.67) in the temporal region, although virtually no changes were noted in other areas.

Correlation of SPECT and MR Imaging Findings. Serial FLAIR images showed cortical hyperintensity, which appeared on POD 1, peaked during PODs 7 and 13, almost returned to normal on POD 56, and demonstrated atrophy in the right temporal lobe on POD 237 (Fig. 4). During transient hyperperfusion and chronic hypoperfusion stages, ^{123}I-iodoamphetamine FLAIR demonstrated marked cortical edema and chronic atrophic change of the affected region, respectively. Subtle diffusion weighted imaging hyperintensity in the affected area was shown between PODs 1 and 7 but disappeared on

POD 35, despite slowly progressive neuronal death documented on ^{123}I-IMZ in the subacute phase (PODs 18–55), during which T1 cortical hyperintensity became prominent (PODs 35–56). The hyperperfusion state of the affected cortex was also confirmed by ^{123}I-IMP SPECT on POD 12. Hyperperfusion of the affected cortex gradually improved and returned to normal, as shown by ^{123}I-IMP SPECT on POD 53. Follow-up MR images showed unique chronological changes such that cortical hyperintensity of the affected cortex appeared on POD 35 and persisted at least until POD 56. Of note, cortical hyperintensity on FLAIR peaked on POD 7 and then gradually decreased in intensity and appeared almost normal on POD 56. In the late chronic stage on POD 237, cortical atrophy with secondary degeneration of the underlying subcortical white matter was noted. No hemorrhagic transformation was noted in the affected regions on CT scans throughout the observation period.

Follow-Up. The patient's cranial nerve III palsy and restlessness gradually improved and he resumed his previous lifestyle 5 months after the second surgery. Eight months after surgery, his Mini-Mental State Examination status returned to normal.

Discussion

We have presented, for the first time, dynamic neuropathological correlations between slowly progressive neuronal death during postischemic hyperperfusion, as shown on ^{123}I-IMZ and ^{123}I-IMP SPECT scans, and emerging cortical laminar necrosis, as shown on T1-weighted MR images, after RA/ECA-MCA bypass grafting for an intracavernous CA aneurysm.

Intracavernous CA aneurysms are usually treated by trapping with/without EC-IC bypass based on presumed tolerance to CA sacrifice.[9] If the CA does not tolerate the balloon test occlusion, a high-flow bypass is indicated when CA sacrifice is performed. Creation of an RA/ECA-MCA bypass graft is a common method of high-flow bypass, and the technical standards and pitfalls have been reported previously.[9,12] The incidence of ischemic complications has been reported to be ~ 10%[9] as a result of early graft occlusion and other causes, but the underlying etiological force, most of which has been considered thromboembolic, remains unproven in most cases.[6,9]

Cortical laminar necrosis is a permanent brain injury characterized on T1-weighted MR images by high-intensity cortical lesions that follow the gyral anatomy of the cerebral cortex. Histopathological and experimental animal studies have demonstrated much more vulnerability of the gray matter than white matter to ischemic necrosis due to hypoperfusion.[19] Previous studies have reported characteristic MR imaging findings of cortical laminar necrosis caused by hypoxic or ischemic brain damage.[7,19] Cortical enhancement on postcontrast T1-weighted images in the subacute stage, suggesting breakdown of the blood-brain barrier, and hyperintense cortical lesions on unenhanced T1-weighted images during the late subacute and early chronic stages were reported to be distributed in the laminae. Cortical laminar necrosis is usually reported
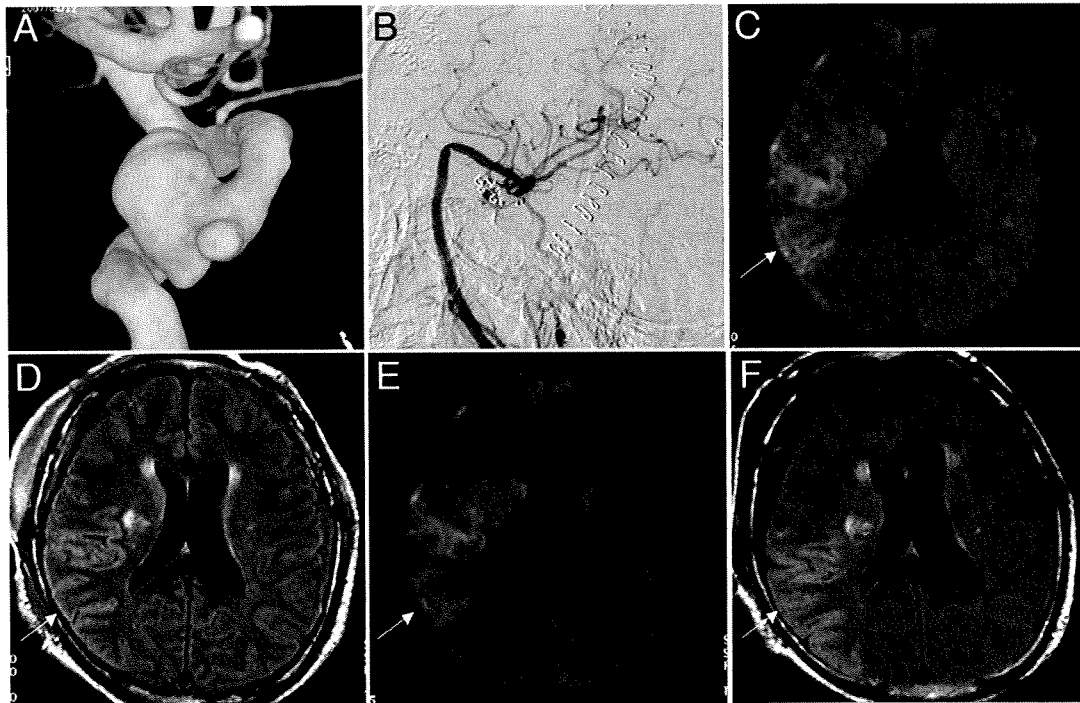
Fig. 1. A: Three-dimensional rotational CA angiogram showing a large intracavernous aneurysm that was treated with radial artery/ECA-MCA bypass grafting. B: Postoperative angiogram. C and D: Diffusion weighted (C) and FLAIR (D) images obtained on POD 1, showing only subtle hyperintensity in the right temporal cortex subjected to temporary clipping. E and F: Diffusion weighted (E) and FLAIR (F) images obtained on POD 7 when the patient became restless. Both of the hyperintensities following a gyral pattern appear slightly increased and well demarcated. Arrows indicate the affected region in the temporal lobe.

to be associated with volume loss of the affected cortex in the chronic stage.[20] Weiller and coworkers[20] have reported finding atrophy of the opercular cortex overlying the subcortical infarct on follow-up MR images ~ 1 year after the insult, suggesting that neuronal loss progresses over time.[13,20] In the present case we observed similar chronological changes of MR imaging signals on T1-weighted and FLAIR images and clearly illustrated the dynamic process of slowly progressive neuronal death associated with postischemic hyperperfusion in the affected cortex, where cortical hyperintensity was emerging in the subacute phase, following subtle diffusion weighted imaging–documented abnormalities in the acute phase.

Hyperperfusion is defined as a significant increase in cerebral blood flow relative to the homologous area of the contralateral hemisphere,[10] and it is known to occur after carotid endarterectomy, EC-IC bypass, and giant aneurysm clipping in patients with chronically impaired cerebrovascular reserve. Previous studies that involved the use of PET or SPECT scanning suggest that hyperperfusion may sometimes be associated with incomplete infarction or selective neuronal loss.[3,13] Flumazenil and ^{123}I-IMZ are markers of central benzodiazepine receptors, part of the GABAergic complex,[2] and ideal markers of periinfarct tissue and incomplete brain infarcts.[16] Sette et al.[16] have reported marked hyperperfusion in the affected territory in ischemic stroke, together with mildly reduced binding of ^{11}C-flumazenil in the acute stage, followed by reduced ^{11}C-flumazenil binding and reduced cerebral metabolic rates of glucose despite unaltered MR imaging findings

in the subacute stage. Nakagawara and colleagues[13] have also reported using ^{123}I-IMZ SPECT in 2 patients with extensive hyperperfusion in the acute stage who exhibited reduced binding of ^{123}I-iomazenil in these areas in the chronic stage despite normal CT findings. The degree and duration of moderate ischemia in the present case was probably in the narrow range, which caused slowly progressive neuronal death without the development of frank infarction involving subcortical white matter, as reported in transient ischemia in animal models.[1] In internal carotid artery occlusive disease, selective neuronal damage was reported to occur beyond the regions of infarcts by hemodynamic ischemia in the chronic stage, as demonstrated on ^{11}C-flumazenil PET scans.[22]

The diagnostic significance of diffusion weighted imaging deserves some mention. Diffusion weighted imaging is considered an accurate predictor of the extent of infarction during the acute or early subacute phase of cerebral ischemia. Heiss et al.[4] compared the probability of cortical infarction by examining flumazenil binding on PET and diffusion weighted images in early ischemic stroke; they concluded that these modalities are comparable in predicting the probability of ischemic cortical infarction. Benzodiazepine receptor activity is a reliable marker of neuronal integrity in the cortex, but movement of water molecules in the extracellular space may be a more variable indicator of tissue damage, such that the false-positive volumes not included in the final infarct were larger for diffusion weighted imaging.[4] Subtle cortical hyperintensity on diffusion weighted imaging of the
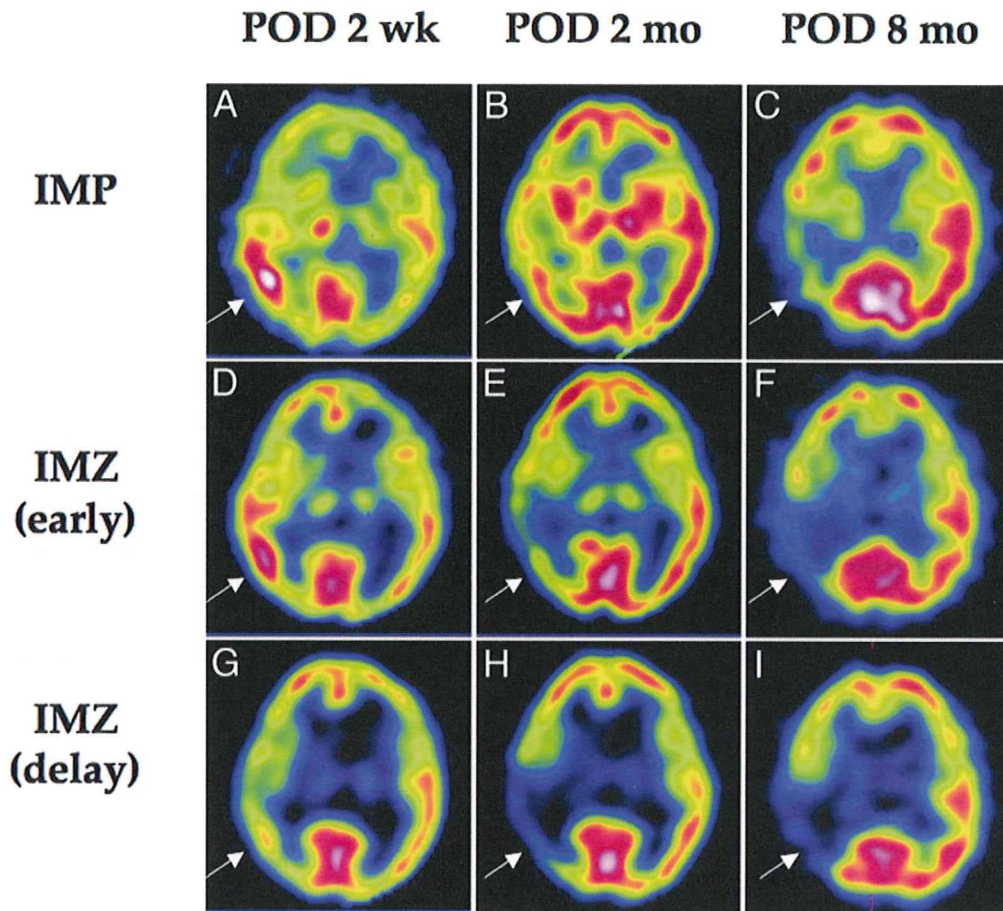
124

POD 2 wk   POD 2 mo   POD 8 mo

FIG. 2. Chronological changes in ^{123}I-IMP and early and delayed ^{123}I-IMZ SPECT images. Iodine-123–labeled iodoamphetamine **(A–C)** and early ^{123}I-IMZ **(D–F)** images similarly showing a transient increase in the subacute stage (POD 2 weeks [POD 2 wk; **A and D**]), followed by progressive decrease in the early and late chronic stages (POD 2 months [POD 2 mo; **B and E**] and 8 months [POD 8 mo; **C and F**]) of uptake in the affected regions. Delayed images of ^{123}I-IMZ **(G–I)** demonstrating delayed decrease of binding of the affected regions between subacute **(G)** and early chronic **(H)** stages, which levels off in the late chronic stage **(I)**. *Arrows* indicate the affected region in the temporal lobe.

affected cortex on PODs 1 and 7 in this case, as reported in global ischemia,[11] disappeared thereafter, despite ongoing neuronal loss during the subacute stage. In animal models, modest signal intensity changes on diffusion weighted imaging precede delayed neuronal necrosis af-

ter transient ischemia.[15] In the present case, however, the rate of decrease of the affected/unaffected ratio, as seen on the delayed ^{123}I-IMZ images, remained constant until POD 55 before and after the first postoperative ^{123}I-IMZ image, if the affected/unaffected ratio before surgery in
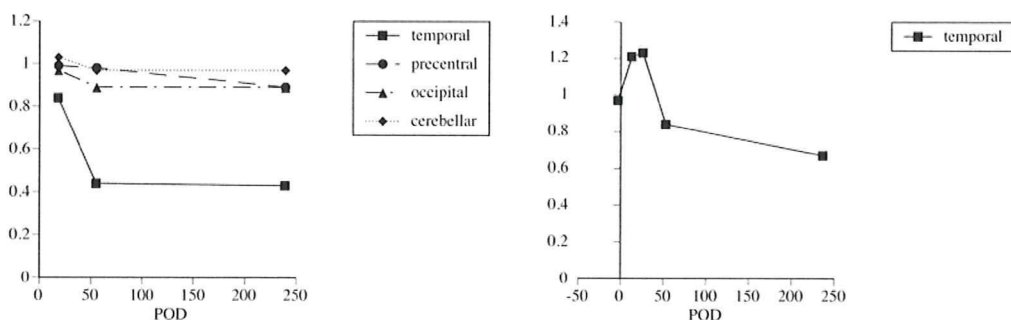

FIG. 3. Line graphs depicting chronological changes of the affected/unaffected count ratio and corresponding regions of interest on delayed ^{123}I-IMZ *(left)* and ^{123}I-IMP *(right)* SPECT images. The count ratio of the affected/unaffected corresponding regions of interest of ^{123}I-IMZ in the different areas (temporal, precentral, occipital, and cerebellar regions) are plotted against PODs. The affected/unaffected ratio of ^{123}I-IMP was plotted only for the affected temporal region.

4

125

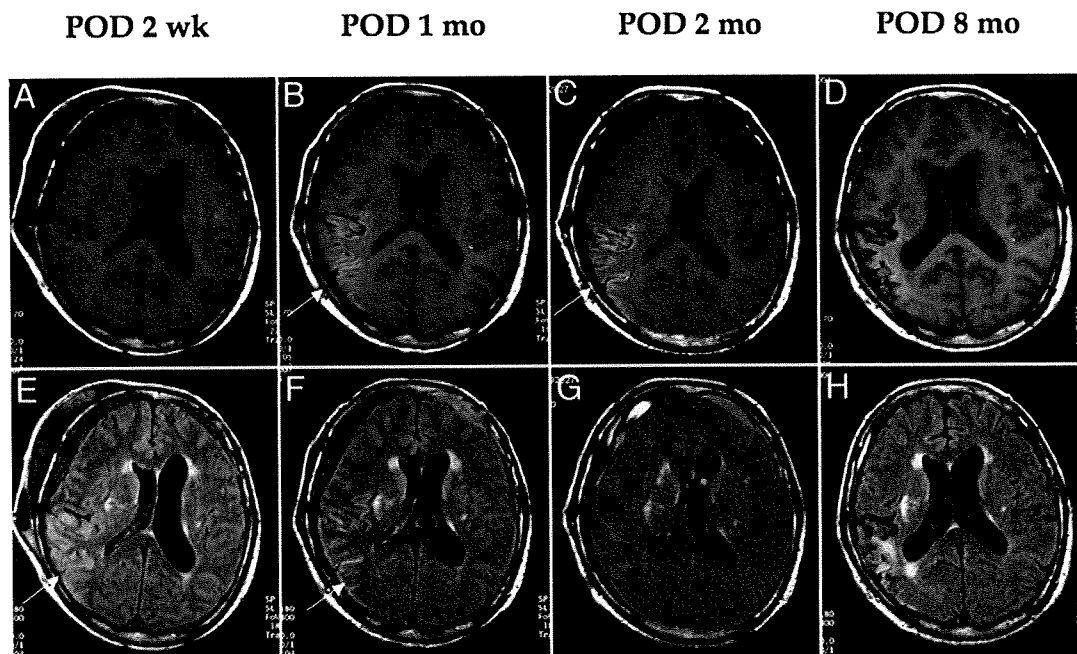**POD 2 wk**   **POD 1 mo**   **POD 2 mo**   **POD 8 mo**

Fig. 4. Chronological changes demonstrated on follow-up MR images. Sagittal T1-weighted images (**A–D**) showing emerging cortical hyperintensity of the affected cortex between 2 weeks after surgery (POD 2 wk; **A**) and 1 month after surgery (POD 1 mo; **B**); the hyperintensity becomes more prominent at 2 months (POD 2 mo; **C**). Cortical laminar necrosis indicates atrophic change in the late chronic stage (**D**). **E–H:** On FLAIR images, cortical hyperintensity gradually decreases from 2 weeks after surgery (POS 2 wk; **E**) to 1 month after surgery (POD 1 mo; **F**) postoperatively and almost disappears by 2 months (POD 2 mo; **G**). In the late chronic stage, cortical atrophy with secondary degeneration of the underlying subcortical white matter is noted (**H**).

the affected cortex was assumed to be 1.0, as in the other areas on the first postoperative ^{123}I-IMZ image. These findings suggest that neuronal loss may not be of delayed onset, but rather slowly progressive after surgery, and diffusion weighted and ^{123}I-IMZ imaging may differ in predicting the probability of slowly progressive neuronal death in cortical laminar necrosis, depending on the interval from the moderate ischemic insult. Iodine-123–labeled IMZ SPECT is useful for examining the dynamic process of slowly progressive neuronal loss, especially in the subacute phase after moderate ischemia. Precise understanding of temporal profiles of neuronal death underlying emerging cortical laminar necrosis should require further accumulation of evidence using ^{123}I-IMZ SPECT.

Previous studies discussed the time permitted for temporary occlusion of the parent artery for aneurysm surgery, especially for an MCA bifurcation aneurysm.[8,12,14] In radial artery/ECA-MCA bypass grafting, however, the time permitted for temporary occlusion of the M_2 segment remains unclear, although the anastomotic time has been recommended to be less than 45 minutes.[12] Obviously, the time threshold for temporary occlusion may depend on multiple factors, such as the use of various neuroprotective agents,[8,14] brain temperature,[21] and extent of collateral flow and cerebrovascular reserve. During the previous 6 years, neither isolated cortical laminar necrosis nor frank infarction due to temporary occlusion had been documented in the other 21 cases treated by high-flow bypass, including 10 patients in whom temporary occlusion lasted more than 45 minutes. In the present case, extremely slow backflow from the distal side of the clamped artery was

a key intraoperative finding, underlying the development of slowly progressive neuronal death. Although previous studies have reported possible preventative measures of ischemic complications related to temporary occlusion, such as excimer laser–assisted nonocclusive anastomosis,[18] the development of small intravascular shunts,[12] and double insurance bypass,[5] there are no widely accepted methods for this purpose.

Conclusions

We have discussed a rare case of slowly progressive neuronal death during postischemic hyperperfusion in cortical laminar necrosis associated with radial artery/ECA-MCA bypass grafting for intracavernous CA aneurysms. We have illustrated the diagnostic importance using of ^{123}I-IMZ SPECT in the subacute phase before emerging characteristic MR imaging findings. Moderate ischemia during temporary occlusion due to poor collateral flow may cause this rare ischemic complication.

References

1. Garcia JH, Liu KF, Ye ZR, Gutierrez JA: Incomplete infarct and delayed neuronal death after transient middle cerebral artery occlusion in rats. **Stroke 28:**2303–2310, 1997
2. Hantraye P, Kaijima M, Prenant C, Guibert B, Sastre J, Crouzel M, et al: Central type benzodiazepine binding sites: a positron emission tomography study in the baboon's brain. **Neurosci Lett 48:**115–120, 1984
3. Heiss WD, Grond M, Thiel A, Ghaemi M, Sobesky J, Rudolf J, et al: Permanent cortical damage detected by flumazenil positron emission tomography in acute stroke. **Stroke 29:**454–461, 1998
4. Heiss WD, Sobesky J, Smekal U, Kracht LW, Lehnhardt FG, Thiel A, et al: Probability of cortical infarction predicted by flumazenil binding and diffusion-weighted imaging signal intensity: a comparative positron emission tomography/magnetic resonance imaging study in early ischemic stroke. **Stroke 35:**1892–1898, 2004
5. Hongo K, Horiuchi T, Nitta J, Tanaka Y, Tada T, Kobayashi S: Double-insurance bypass for internal carotid artery aneurysm surgery. **Neurosurgery 52:**597–602, 2003
6. Jafar JJ, Russell SM, Woo HH: Treatment of giant intracranial aneurysms with saphenous vein extracranial-to-intracranial bypass grafting: indications, operative technique, and results in 29 patients. **Neurosurgery 51:**138–146, 2002
7. Komiyama M, Nakajima H, Nishikawa M, Yasui T: Serial MR observation of cortical laminar necrosis caused by brain infarction. **Neuroradiology 40:**771–777, 1998
8. Lavine SD, Masri LS, Levy ML, Giannotta SL: Temporary occlusion of the middle cerebral artery in intracranial aneurysm surgery: time limitation and advantage of brain protection. **J Neurosurg 87:**817–824, 1997
9. Lawton MT, Hamilton MG, Morcos JJ, Spetzler RF: Revascularization and aneurysm surgery: current techniques, indications, and outcome. **Neurosurgery 38:**83–84, 1996
10. Marchal G, Young AR, Baron JC: Early postischemic hyperperfusion: pathophysiologic insights from positron emission tomography. **J Cereb Blood Flow Metab 19:**467–482, 1999
11. McKinney AM, Teksam M, Felice R, Casey SO, Cranford R, Truwit CL, et al: Diffusion-weighted imaging in the setting of diffuse cortical laminar necrosis and hypoxic-ischemic encephalopathy. **AJNR Am J Neuroradiol 25:**1659–1665, 2004
12. Mohit AA, Sekhar LN, Natarajan SK, Britz GW, Ghodke B: High-flow bypass grafts in the management of complex intracranial aneurysms. **Neurosurgery 60 (2 Suppl 1):**ONS105–ONS123, 2007
13. Nakagawara J, Sperling B, Lassen NA: Incomplete brain infarction of reperfused cortex may be quantitated with iomazenil. **Stroke 28:**124–132, 1997
14. Ogilvy CS, Carter BS, Kaplan S, Rich C, Crowell RM: Temporary vessel occlusion for aneurysm surgery: risk factors for stroke in patients protected by induced hypothermia and hypertension and intravenous mannitol administration. **J Neurosurg 84:**785–791, 1996
15. Rojas S, Martin A, Justicia C, Falcon C, Bargallo N, Chamorro A, et al: Modest MRI signal intensity changes precede delayed cortical necrosis after transient focal ischemia in the rat. **Stroke 37:**1525–1532, 2006
16. Sette G, Baron JC, Young AR, Miyazawa H, Tillet I, Barre L, et al: In vivo mapping of brain benzodiazepine receptor changes by positron emission tomography after focal ischemia in the anesthetized baboon. **Stroke 24:**2046–2048, 1993
17. Siskas N, Lefkopoulos A, Ioannidis I, Charitandi A, Dimitriadis AS: Cortical laminar necrosis in brain infarcts: serial MRI. **Neuroradiology 45:**283–288, 2003
18. Streefkerk HJ, Bremmer JP, Tulleken CA: The ELANA technique: high flow revascularization of the brain. **Acta Neurochir Suppl 94:**143–148, 2005
19. Takahashi S, Higano S, Ishii K, Matsumoto K, Sakamoto K, Iwasaki Y, et al: Hypoxic brain damage: cortical laminar necrosis and delayed changes in white matter at sequential MR imaging. **Radiology 189:**449–456, 1993
20. Weiller C, Willmes K, Reiche W, Thron A, Isensee C, Buell U, et al: The case of aphasia or neglect after striatocapsular infarction. **Brain 116:**1509–1525, 1993
21. Westermaier T, Zausinger S, Baethmann A, Steiger HJ, Schmid-Elsaesser R: No additional neuroprotection provided by barbiturate-induced burst suppression under mild hypothermic conditions in rats subjected to reversible focal ischemia. **J Neurosurg 93:**835–844, 2000
22. Yamauchi H, Kudoh T, Kishibe Y, Iwasaki J, Kagawa S: Selective neuronal damage and borderzone infarction in carotid artery occlusive disease: a 11C-flumazenil PET study. **J Nucl Med 46:**1973–1979, 2005

Hyperintense Plaque With Noncontrast T1-Weighted Magnetic Resonance Coronary Plaque Imaging Leading to Acute Coronary Syndrome

Atsushi Tanaka, MD; Tomohiro Kawasaki, MD; Teruo Noguchi, MD; Shoichi Koga, MD; Yoshihiro Hiramatsu, MD; Takaya Fukuyama, MD; Nobuhiko Koga, MD

A 73-year-old diabetic man underwent multislice computed tomography (MSCT) and noncontrast T1-weighted (T1W) magnetic resonance imaging (MRI) for the evaluation of atypical chest discomfort after an exercise ECG was nondiagnostic. The MSCT demonstrated a low-density positive remodeling plaque and spotty calcification without significant stenosis in the proximal segment of the right coronary artery (Figure 1A and 1B). Noncontrast T1W MRI, using a 1.5-T MR system (Intera, Philips Medical Systems, Best, the Netherlands), revealed a hyperintense plaque (HIP) in the right coronary artery in an area corresponding to the plaque visualized by MSCT (Figure 1C and 1D). With clear evidence of atherosclerotic disease, the patient
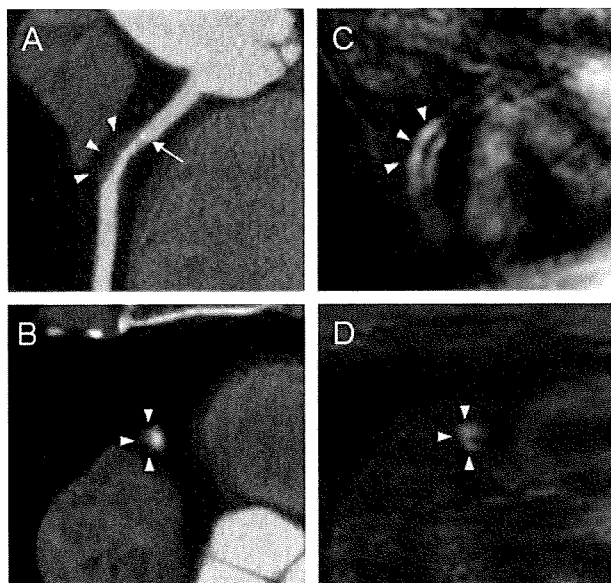

Figure 2. Right coronary angiography revealed an occlusion of the proximal segment of the right coronary artery (A). On intravascular ultrasound examination (B), a near-circumferential attenuation (arrowheads) was observed at the culprit lesion, corresponding with the plaque observed both by multislice computed tomography and by noncontrast T1-weighted magnetic resonance imaging.

was given glimepiride and voglibose with recommendations for strict diet therapy for treatment of diabetes mellitus; he continued to take aspirin. One year after these examinations, the patient presented with sudden-onset crushing chest pain at our emergency room. Despite the modifications to his medications, his coronary risk factors had not improved (hemoglobin A_{1c}, 7.1–6.4%, low-density lipoprotein cholesterol, 124–110 mg/dL; high-density lipoprotein cholesterol, 34–32 mg/dL). On admission, an ECG showed ST-segment elevation in leads II, III, and aV_F. Emergent coronary angiography revealed an obstructive lesion in the proximal segment of the right coronary artery in a region corresponding to the HIP previously identified by MRI (Figure 2A). Intravascular ultrasound confirmed extensive attenuation (Figure 2B) at that segment, and a bare metal stent was successfully implanted with a distal protection device. After stent implantation, a large amount of debris was collected.

Recently, Kawasaki et al[1] reported that the presence of HIP on noncontrast T1W MRI is associated with positive coronary remodeling, low CT density, and ultrasound attenuation by MSCT or intravascular ultrasound. However, it is unknown whether HIP has a greater potential for plaque rupture and subsequent acute coronary syndrome. To our knowledge,

Figure 1. Multislice computed tomography (A, curved multiplanar reconstruction; B, horizontal) demonstrates low-density plaque (−36 Hounsfield units, remodeling index 1.6, arrowheads) with spotty calcification (arrow) in the proximal segment of the right coronary artery. On the corresponding noncontrast T1-weighted magnetic resonance imaging (C, oblique image; D, horizontal), this low-density plaque was visualized as a hyperintense lesion (arrowheads).
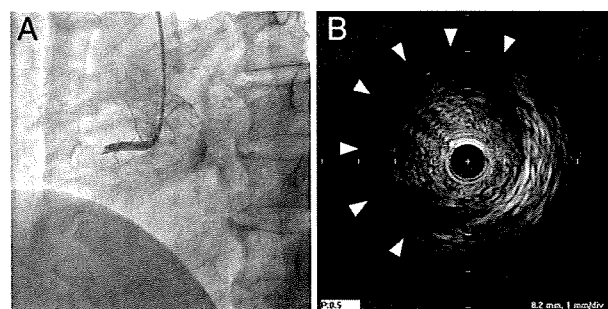
DOI: 10.1161/CIRCULATIONAHA.108.895482

this is the first report documenting the progression of HIP to acute coronary syndrome. Thus, HIP detected by noncontrast T1W MRI has the potential to identify vulnerable coronary lesions.

Disclosures

None.

Reference

1. Kawasaki T, Koga S, Koga N, Noguchi T, Tanaka H, Koga H, Serikawa T, Orita Y, Ikeda S, Mito T, Goto Y, Shintani Y, Tanaka A, Fukuyama T. Characterization of hyperintense plaque with non-contrast T1-weighted cardiovascular magnetic resonance coronary plaque imaging: comparison with multislice computed tomography and intravascular ultrasound. *J Am Coll Cardiol Cardiovasc Imaging.* 2009;6:720–728.

Characterization of Hyperintense Plaque With Noncontrast T$_1$-Weighted Cardiac Magnetic Resonance Coronary Plaque Imaging

Comparison With Multislice Computed Tomography and Intravascular Ultrasound

Tomohiro Kawasaki, MD,* Shoichi Koga, MD,† Nobuhiko Koga, MD,*
Teruo Noguchi, MD,‡ Hidenori Tanaka, MD,* Hisashi Koga, MD,* Takeshi Serikawa, MD,*
Yoshiya Orita, MD,* Shinsuke Ikeda, MD,* Takahiro Mito, MD,* Yoshitaka Goto, MD,*
Yoshiaki Shintani, MD,* Atsushi Tanaka, MD,† Takaya Fukuyama, MD*

Kurume, and Suita, Japan

OBJECTIVES This study sought to characterize coronary hyperintense plaques (HIP) using noncontrast T$_1$-weighted imaging (T1WI) in cardiac magnetic resonance, which was then compared with multislice computed tomography and intravascular ultrasound.

BACKGROUND Carotid plaque components such as intraplaque hemorrhages and/or lipid-rich necrotic cores can be detected as HIP by noncontrast T1WI. Although coronary HIPs have been successfully detected using this technique, the properties of hyperintense signals in coronary plaques have not yet been systematically evaluated.

METHODS Thirty-eight lesions from 37 patients with angina pectoris who demonstrated >70% coronary stenosis on multislice computed tomography were evaluated by noncontrast T1WI using a 1.5-T magnetic resonance imager, and 25 lesions were evaluated by intravascular ultrasound. Signal intensity of coronary plaque to cardiac muscle ratio >1.0 was defined as HIP. We divided 25 lesions into the 2 groups, according to the presence or absence of HIP: HIP (n = 18) and non-HIP (n = 7) groups.

RESULTS In comparison with the non-HIP group, the HIP group demonstrated significantly higher coronary plaque to cardiac muscle ratio (1.7 ± 0.7 vs. 0.9 ± 0.1, p < 0.01), higher frequency of positive remodeling as observed by both multislice computed tomography (89% vs. 0%, p<0.0001) and intravascular ultrasound (94% vs. 14%, p < 0.001) and ultrasound attenuation (100% vs. 14.3%, p < 0.0001). The frequency of spotty calcification tended to be higher in HIP (89% vs. 50%, p = 0.079). The HIP group also exhibited a significantly lower computed tomography density (–23.2 ± 20.7 Hounsfield units [HU] vs. 9.6 ± 20.5 HU, p < 0.01). In addition, the incidence of transient slow-flow phenomena was significantly higher in the HIP group than in the non-HIP group (83% vs. 14%, p < 0.01).

CONCLUSIONS The typical HIP case was associated with ultrasound attenuation, positive remodeling, remarkably low computed tomography density, and a high incidence of slow-flow phenomena. Noncontrast T1WI in cardiac magnetic resonance imaging may be useful for the assessment of coronary plaque characterization in patients with coronary artery disease. (J Am Coll Cardiol Img 2009;2:720–8) © 2009 by the American College of Cardiology Foundation

Cardiac magnetic resonance (CMR) imaging (1–3) and multislice computed tomography (MSCT) (4–7) are attracting attention as new noninvasive imaging techniques for coronary plaque visualization. Noncontrast T_1-weighted imaging (T1WI) in CMR enables the identification of the thickened coronary wall (1–3). In addition, contrast-enhanced CMR allows us to identify areas of delayed enhancement that correlate with the severity of atherosclerosis as measured by MSCT and quantitative coronary angiography (8).

In carotid plaques, high signals on inversion recovery-based 3-dimensional T1WI are associated with complicated plaques (type VI as proposed by the American Heart Association) (9) and with recent ischemic cerebrovascular events (10,11). Thus, CMR with T1WI is able to successfully identify vulnerable carotid plaques. Although coronary plaque imaging by noncontrast- and contrast-enhanced T1WI has been successfully demonstrated, and coronary plaques can be visualized as hyperintense signal areas, the properties of hyperintense signals in coronary plaques detected by T1WI have not yet been systematically evaluated.

To address this, we sought to characterize hyperintense coronary plaques visualized by noncontrast T1WI in CMR to compare findings obtained by MSCT and intravascular ultrasound (IVUS).

METHODS

Study population. Thirty-seven consecutive angina pectoris patients with a total of 38 lesions were enrolled. In all of these patients, significant coronary stenosis (>70%) was detected on MSCT; all were scheduled for elective percutaneous coronary intervention (PCI) between February 2007 and November 2007. All 38 lesions (37 patients) had been evaluated by noncontrast T1WI in CMR before PCI. Twenty-eight lesions from 27 patients contained areas with hyperintense signals, corresponding to the target lesions on MSCT (defined as hyperintense plaque [HIP]). In contrast, 10 lesions from the remaining 10 patients contained areas without hyperintense signals (defined as non-HIP). We excluded 13 lesions from 13 patients, 10 HIP and 3 non-HIP, who had not undergone IVUS examination duri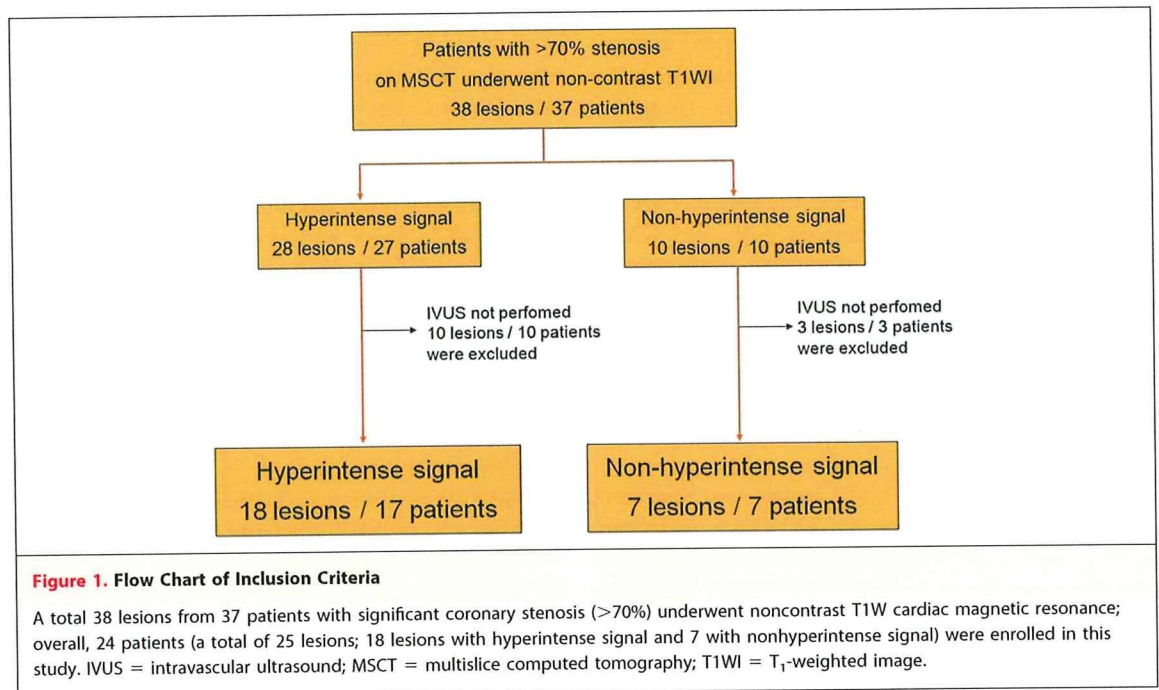ng PCI. Thus, 25 lesions from 24 patients (18 HIP and 7 non-HIP) were examined in this study (Fig. 1). Both MSCT and CMR were performed within a month before the IVUS examination. The study protocol was approved by the Institutional Board on Clinical Investigations at Shin-Koga Hospital. Information regarding this study was provided either orally or in written form to all subjects, and written informed consent was obtained from each subject.

CMR coronary plaque imaging. Coronary plaque imaging was obtained with a 1.5-T MR imager (Intera, Philips Medical Systems, Best, the Netherlands) using 5-element cardiac coils. When heart rates were more than 65 beats/min, the rates were adjusted by administration of 20 to 40 mg of metoprolol 30 min before imaging. Nitroglycerin (0.3 mg) was also administered sublingually immediately before taking images to obtain high-quality CMR images. The survey images were focused around the heart, and the reference images were taken under free breathing to improve the sensitivity of parallel imaging. Coronary plaque images were obtained when patients were breathing freely, with the use of a 3-dimensional, T1W inversion-recovery gradient-echo sequence with fat-suppressed and radial k-space sampling (repetition time: shortest $\fallingdotseq$ 4.7 ms, echo time: shortest $\fallingdotseq$ 1.37 ms, flip angle: 20°, excitations per cardiac cycle: 15 to 45, SENSE factor: 2.5, number of excitations: 2, navigator gating window: 5 mm, no drift correction, field of view: 300 × 270 × 112 mm, acquisition matrices: 224 × 224, reconstruction matrices: 512 × 512 × 140). Spatial resolution was 1.34 × 1.34 × 1.6 mm. The same value was set for the acquisition window as in the coronary CMR. The acquisition window was set, according to the movement of the heart, for the time during the diastolic phase at which the heart moves the least. The movement of the heart was confirmed using cine-MR images that had been taken previously. The cine-MR images were obtained with a steady-state sequence as the patient was free breathing (repetition time: 2.6 ms, echo time: 1.3 ms, flip angle: 60°, field of view: 360 × 324 × 7 mm, acquisition matrix: 192 × 192, cardiac phases: 50, SENSE factor: 3.0, imaging time: 2 s).

A coronary CMR image analysis was performed by 2 technicians who were blinded to the plaque information obtained by MSCT. In the coronary CMR image obtained, if the areas that corre-

ABBREVIATIONS AND ACRONYMS

CMR = cardiac magnetic resonance

HIP = hyperintense plaque

IVUS = intravascular ultrasound

MSCT = multislice computed tomography

PCI = percutaneous coronary intervention

PMR = coronary plaque to cardiac muscle ratio

RI = remodeling index

T1WI = T_1-weighted imaging

Figure 1. Flow Chart of Inclusion Criteria

A total 38 lesions from 37 patients with significant coronary stenosis (>70%) underwent noncontrast T1W cardiac magnetic resonance; overall, 24 patients (a total of 25 lesions; 18 lesions with hyperintense signal and 7 with nonhyperintense signal) were enrolled in this study. IVUS = intravascular ultrasound; MSCT = multislice computed tomography; T1WI = T_1-weighted image.

sponded to the target lesion on MSCT were confirmed, then the signal intensity of coronary plaque to muscle ratio (PMR) (PMR was defined as the signal intensity of the coronary plaque divided by the signal intensity of the cardiac muscle) was calculated. Areas with PMR >1.0 were defined as HIP, whereas areas with PMR ≤1.0 were defined as non-HIP. The representative cases with HIP and with non-HIP are shown in Figure 2. The signal intensity of the myocardium was measured at a site of the left ventricle near the coronary plaque.

Coronary Computed Tomography (CT) angiography. Coronary CT angiography was performed using MSCT (LightSpeed Volume CT, GE Healthcare, Milwaukee, Wisconsin). A coronary image was acquired with 64 × 0.625-mm slice collimation, a gantry rotation time of 0.35 ms, table feed: 7.2 to 8.2 mm/rotation, tube energy: 120 kV, and effective tube current: 280 mA. The total amount of contrast media (50.1 ± 5.1 ml iopamidol, 370 mgl/ml) (Schering AG, Berlin, Germany) was injected intravenously at a rate of 3.5 to 4.0ml/s. Transaxial images were reconstructed using a medium sharp conventional kernel/standard smooth kernel (B25F) and sharp kernel (B46F). The image matrix was 512 × 512 pixels, with a slice thickness of 0.75 mm and an increment of 0.4 mm using an electrocardiography-gated half-scan algorithm with a resulting temporal resolution of 165 ms in the center of rotation. Image reconstruction was retrospectively gated to the

electrocardiogram. The patients with a heart rate >70 beats/min received 20 mg of metoprolol orally 60 min before scanning, and almost all of the patients received 0.3 mg of nitroglycerin sublingually just before scanning. Image reconstruction was performed using a 3-dimensional workstation (Advantage Workstation version 4.2, GE Healthcare). A focal multiplanar reconstruction image and cross-sectional image at the lesion were used for the assessment of coronary plaque morphology, including vessel remodeling index (RI), the minimum CT density of the plaques (expressed by Hounsfield units [HU]), and spotty calcification. The RI on MSCT was calculated by dividing the cross-sectional vessel area at the lesion by the mean of the 2 reference areas, which were obtained within 5 mm proximal to and 5 mm distal to the lesion. Positive remodeling was defined as RI >1.10 (12). Spotty calcification was defined as features <3 mm in size on a focal multiplanar reconstruction image and cross-sectional image in the lesion (13,14). An MSCT image analysis was performed by 2 technicians who were blinded to the plaque information obtained by CMR and IVUS.

IVUS image. The IVUS image was obtained before the PCI within 1 or 2 weeks after the CMR and MSCT. The IVUS system used a commercially available 40-MHz IVUS catheter (Atlantis Pro 2.9-F, Boston Scientific, Natick, Massachusetts) with 0.5 mm/s auto-pullback. The manual con-
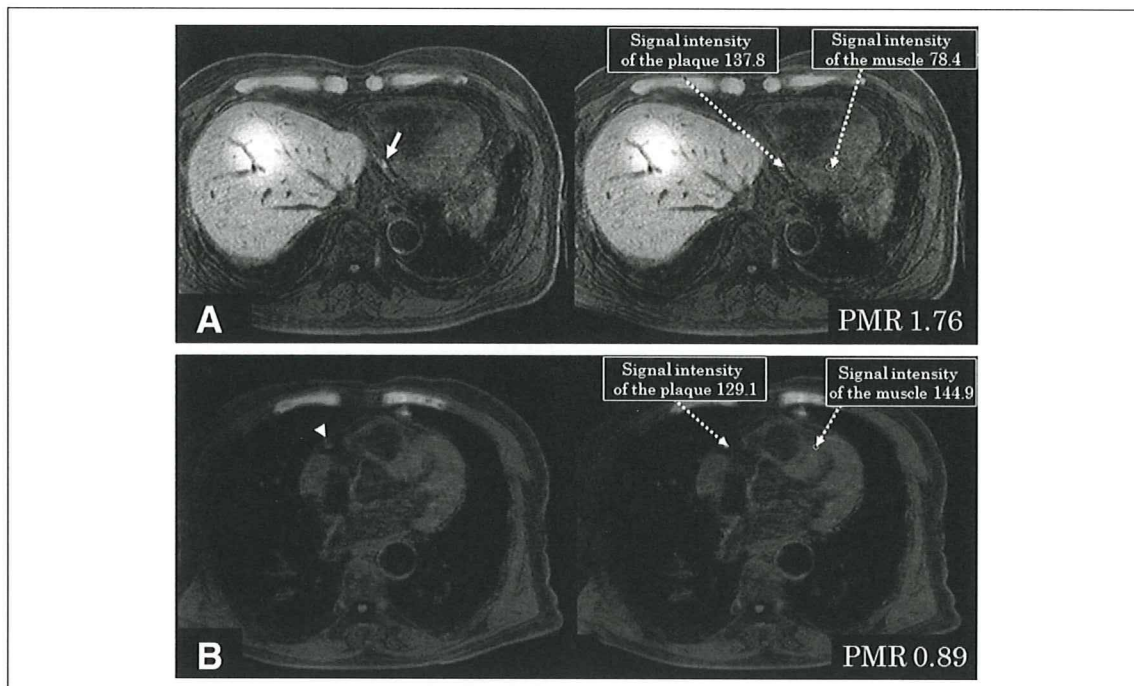
Figure 2. Representative Case With and Without HIP

(A) Representative case with hyperintense area (white arrow) at distal right coronary artery (left panel). In this case, the intensity of coronary plaque to cardiac muscle ratio (PMR) was 1.76 and it was classified as a hyperintense plaque (HIP) (right panel). (B) Representative case without hyperintense signal area (arrowhead) at proximal right coronary artery (left panel). The PMR was 0.89 and it was classified as non-HIP (right panel).

tour detection of the external elastic membrane was performed at the lesion and at the proximal reference site, and the RI was then calculated as the external elastic membrane of the lesion divided by the external elastic membrane of the proximal reference site, as previously described (15,16). Positive remodeling was defined as RI >1.05 (17). In addition, the plaque was checked to determine whether ultrasound attenuation was present. Ultrasound attenuation was defined as backward attenuation of signals behind the coronary atheroma without echogenic deposits or calcium within the plaque (18). The grade of ultrasound attenuation was classified into 3 categories according to the arc of the attenuation as follows: − = no attenuation; + = attenuation <180°; ++ = attenuation ≥180°(18).

Statistical analysis. Continuous data were summarized as mean ± SD. Categorical data were summarized as counts and percentages. The comparison of the plaque characteristics between the HIP and non-HIP groups was made using an unpaired t test in continuous data and Fisher exact tests in categorical data. All interpretations of CMR, MSCT, and IVUS imaging were performed in a blinded manner. Interobserver agreement was calculated

using kappa statistics. A value of $p < 0.05$ was considered statistically significant.

RESULTS

Of all 25 lesions used in the study, 18 lesions (72%) were classified as HIP and 7 lesions (28%) were classified as non-HIP. The baseline characteristics of those 25 lesions (from 24 patients) are shown in Table 1. Other than in target coronary vessel involvement, there was no statistically significant difference in patient clinical characteristics between HIP and non-HIP lesions. The relationship between the HIP/non-HIP lesions on noncontrast T1WI and the plaque morphology obtained by MSCT and IVUS is shown in Table 2 and is summarized in Table 3. The averaged PMR in HIP lesions was significantly higher than in non-HIP lesions (1.70 ± 0.71 vs. 0.90 ± 0.08, $p < 0.001$). Positive remodeling on MSCT was observed in 16 (89%) of the 18 patients with HIP as opposed to 0 (0%) of the 7 patients with non-HIP. In addition, minimal CT density was significantly lower in HIP lesions (−23.2 ± 20.7 HU vs. 9.6 ± 20.5 HU, $p < 0.01$).

Table 1. Baseline Clinical and Angiographic Characteristics

	HIP (n = 17)	Non-HIP (n = 7)	p Value
Age, yrs, mean ± SD	66 ± 9	66 ± 12	NS
Sex, male/female	14/3	4/3	NS
Diagnosis			
AP/UAP	14/3	5/2	NS
Number of CAD			
SVD/MVD	9/8	3/4	NS
Coronary risk factors, n (%)			
Hypertension	14 (82.4%)	3 (42.9%)	NS
Hypercholesterolemia	13 (76.5%)	4 (57.1%)	NS
Diabetes mellitus	7 (41.2%)	2 (28.6%)	NS
Current smoking	4 (23.5%)	3 (42.9%)	NS
Target vessel, n (%)			0.047
LAD	11 (61.1%)	4 (57.1%)	
LCX	0 (0%)	2 (28.6%)	
RCA	7 (38.9%)	1 (14.3%)	

AP = angina pectoris; CAD=coronary artery disease; HIP = hyperintense plaque; LAD = left descending artery; LCX = left circumflex artery; MVD = multivessel disease; NS = not significant; RCA = right coronary artery; SD = standard deviation; SVD = single vessel disease; UAP = unstable angina pectoris.

The frequency of spotty calcification tended to be higher in HIP lesions (89% vs. 50%, p = 0.079). Positive remodeling based on IVUS examinations was observed in 17 (94%) of the 18 patients with HIP, which is significantly higher than in non-HIP patients (14%, p < 0.0001). The frequency of ultrasound attenuation was significantly higher in HIP lesions (100% vs. 14%, p < 0.0001). The kappa statistics for interobserver agreement for ultrasound attenuation was 0.87 (substantial agreement). Transient coronary slow-flow phenomena were observed immediately after either first balloon dilation or stent implantation in 15 (83%) of the 18 patients with HIP, which is significantly higher than in non-HIP patients (14%, p < 0.01). Comparisons of CMR with both MSCT and IVUS of representative cases with HIP are shown in Figures 3 and 4.

DISCUSSION

This is the first report to systematically evaluate the components of HIP detected by noncontrast T1WI in CMR using both MSCT and IVUS examinations. Our findings demonstrate that typical coronary HIP is associated with a high frequency of ultrasound attenuation and positive remodeling, remarkably low CT density, and a high incidence of transient slow-flow phenomena. These results indicate that noncontrast T1WI in CMR is a useful technique for characterization of coronary plaque components.

Coronary plaque imaging with noncontrast T1WI was first reported by Maintz et al. (19) and Yeon et al. (8). These investigators speculated that a hyperintense signal in coronary plaques on noncontrast T1WI indicates the presence of mural or intraplaque thrombus containing methemoglobin. However, these investigators did not systematically evaluate the properties of hyperintense signals in coronary plaques. In our study, the properties of the HIP on noncontrast T1W CMR were examined by using both MSCT and IVUS imaging obtained before PCI. We used noncontrast T1W inversion-recovery and fat-suppressed 3-dimensional black-blood gradient-echo sequence on a 1.5-T MR system. This technique has successfully yielded a description of HIP similar to those observed in the carotid artery (9,20). Recently, our group showed that by using this technique HIP could be observed in the area corresponding to the low-density coronary plaques with positive coronary remodeling observed by MSCT.

Comparison between CMR images and MSCT and IVUS. Using MSCT, HIP has a significantly higher frequency of positive remodeling and lower CT density in comparison with non-HIP. The frequency of spotty calcification tended to be higher in HIP. Noncalcified plaques <30 HU on MSCT correlated with the presence of a lipid-rich necrotic core (21); the presence of 3 features of coronary plaque on MSCT (positive remodeling, noncalcified plaque <30 HU, and spotty calcification) provided a high level of confidence for the characterization of vulnerable plaques associated with acute coronary syndrome (14). In the present study, all 18 HIP cases displayed significantly lower CT values, and 80% of them presented on MSCT with the aforementioned 3 typical features; in contrast, none of the non-HIP cases exhibited those 3 features. These findings suggest that observation of HIP on noncontrast T1WI may reflect the potential for plaque vulnerability.

In comparisons with IVUS images, HIP also has a significantly higher frequency of positive remodeling and ultrasound attenuation than non-HIP. In this study, positive coronary remodeling was observed with a higher frequency in HIP on both MSCT and IVUS. Positive remodeling associated with a plaque is thought to reflect a compensatory enlargement to avoid the decrease of the coronary lumen (22). On the other hand, Varnava et al. (23) performed a pathological

134

Table 2. Lesion Characteristics and Clinical Results of HIP/Non-HIP on CMR, MSCT, and IVUS

Lesion	Target		PMR	PR	RI	MSCT Minimum CT Density (HU)	MSCT Spotty Calcification	IVUS UA*	IVUS PR	IVUS RI	Slow Flow
HIP											
1	LAD	Seg 6	3.93	Yes	1.30	−50	Yes	++	Yes	1.18	Yes
2	LAD	Seg 6	2.63	Yes	1.27	−32	No	++	Yes	1.29	Yes
3	LAD	Seg 6	2.09	Yes	1.18	−19	Yes	++	Yes	1.15	Yes
4	RCA	Seg 3	2.03	Yes	1.17	−66	Yes	+	Yes	1.13	Yes
5	LAD	Seg 6	1.98	No	1.03	−26	Yes	+	Yes	1.14	No
6	RCA	Seg 1	1.78	Yes	1.27	−19	Yes	++	Yes	1.11	No
7	RCA	Seg 3	1.78	Yes	1.15	−7	Yes	++	Yes	1.13	Yes
8	RCA	Seg 3	1.76	Yes	1.24	−44	Yes	+	Yes	1.11	Yes
9	LAD	Seg 6	1.67	Yes	1.24	−3	No	+	Yes	1.15	Yes
10	RCA	Seg 3	1.56	Yes	1.27	−12	Yes	+	Yes	1.26	Yes
11	LAD	Seg 7	1.45	Yes	1.12	−42	Yes	+	Yes	1.08	Yes
12	RCA	Seg 2	1.27	Yes	1.20	−16	Yes	++	Yes	1.19	Yes
13	RCA	Seg 1	1.24	Yes	1.10	−18	Yes	++	Yes	1.16	Yes
14	LAD	Seg 7	1.14	No	1.04	0	Yes	+	No	1.02	Yes
15	LAD	Seg 6	1.12	Yes	1.27	−41	Yes	+	Yes	1.21	Yes
16	LAD	Seg 6	1.05	Yes	1.13	−37	Yes	++	Yes	1.09	No
17	LAD	Seg 6	1.05	Yes	1.26	2	Yes	+	Yes	1.17	Yes
18	LAD	Seg 6	1.01	Yes	1.19	12	Yes	++	Yes	1.08	Yes
Non-HIP											
1	LAD	Seg 6	0.98	No	1.07	−21	No†	+	Yes	1.09	Yes
2	RCA	Seg 2	0.97	No	0.96	28	Yes	−	No	0.85	No
3	LAD	Seg 7	0.94	No	0.97	8	No	−	No	0.93	No
4	LAD	Seg 7	0.94	No	0.99	12	Yes	−	No	0.82	No
5	LCX	Seg11	0.89	No	0.99	37	Yes	−	No	0.95	No
6	LAD	Seg 6	0.86	No	0.97	15	No	−	No	0.88	No
7	LCX	Seg 15	0.74	No	0.92	−12	No	−	No	0.73	No

*Ultrasound attenuation category: − = no ultrasound attenuation, + = arc of attenuation <180°, ++ = arc of attenuation ≥180°. †Large calcification was observed.
CMR = cardiac magnetic resonance; CT = computed tomography; HU = Hounsfield unit; IVUS = intravascular ultrasound; MSCT = multislice computed tomography; PMR = intensity of coronary plaque to cardiac muscle ratio; PR = positive remodeling; RI = remodeling index; Seg = segment; UA = ultrasound attenuation; other abbreviations as in Table 1.

examination of positive remodeling plaques and reported that they have higher lipid content and macrophage count; these 2 findings are recognized pathological markers for plaque vulnerability. Furthermore, positive remodeling plaques have a larger fibro-fatty component according to the IVUS radiofrequency data (24,25); these positive remodeling plaques are observed frequently in patients with acute coronary syndrome (14–16). Therefore, positive coronary remodeling is thought to have a potential for plaque vulnerability. In this study, the rate of positive remodeling was very high. However, in previous studies, the rate of positive remodeling of lesions subjected to elective PCI has not been very high (15,26,27). This discrepancy may relate to the characteristics of HIP. As we have already mentioned, HIP is strongly associated with a remarkably low CT density and a high frequency of

Table 3. Characteristics in Hyperintense and Normointense Plaque

	HIP (n = 18)	Non-HIP (n = 7)	p Value
PMR	1.70 ± 0.71	0.90 ± 0.08	0.0081
MSCT			
Positive remodeling, yes/no	16/2	0/7	<0.0001
RI	1.19 ± 0.08	0.98 ± 0.05	<0.0001
Minimal CT density, HU	−23.2 ± 20.7	9.6 ± 20.5	0.0016
Spotty calcification, yes/no	16/2	3/3*	0.079
IVUS			
Positive remodeling, yes/no	17/1	1/6	<0.001
RI	1.15 ± 0.07	0.89 ± 0.11	<0.0001
Ultrasound attenuation, yes/no	18/0	1/6	<0.0001
Slow flow phenomenon, yes/no	15/3	1/6	0.003

*One excluded because of large calcification.
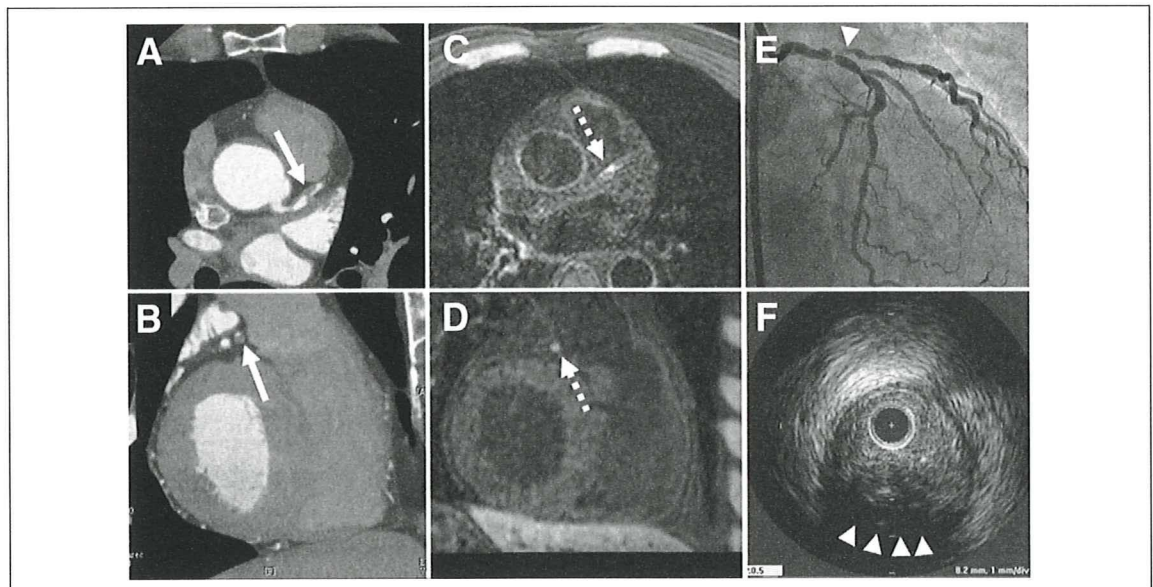Abbreviations as in Tables 1 and 2.

135

Figure 3. Representative Case of HIP in the Proximal LAD

A 60-year-old patient with a severe coronary stenosis in the proximal left descending artery (LAD) is shown. Multislice computed tomography (MSCT) (**A:** horizontal, **B:** sagittal) demonstrates the low-density positive remodeling plaque (–32 Hounsfield units, remodeling index: 1.27) (**arrow**) with severe coronary stenosis in the proximal LAD. On the corresponding cardiac magnetic resonance (CMR) (**C:** horizontal, **D:** sagittal), this low-density plaque was visualized as a "hyperintense spot" (**dashed arrow**). On the coronary angiography, severe coronary stenosis was observed (**E**) (**arrowhead**), and on IVUS examination (**F**), positive remodeling plaque (remodeling index: 1.29) with ultrasound attenuation (**arrowheads**) was observed in the proximal LAD, corresponding with the plaque observed by both MSCT and CMR. HIP = hyperintense plaque; IVUS = intravascular ultrasound.
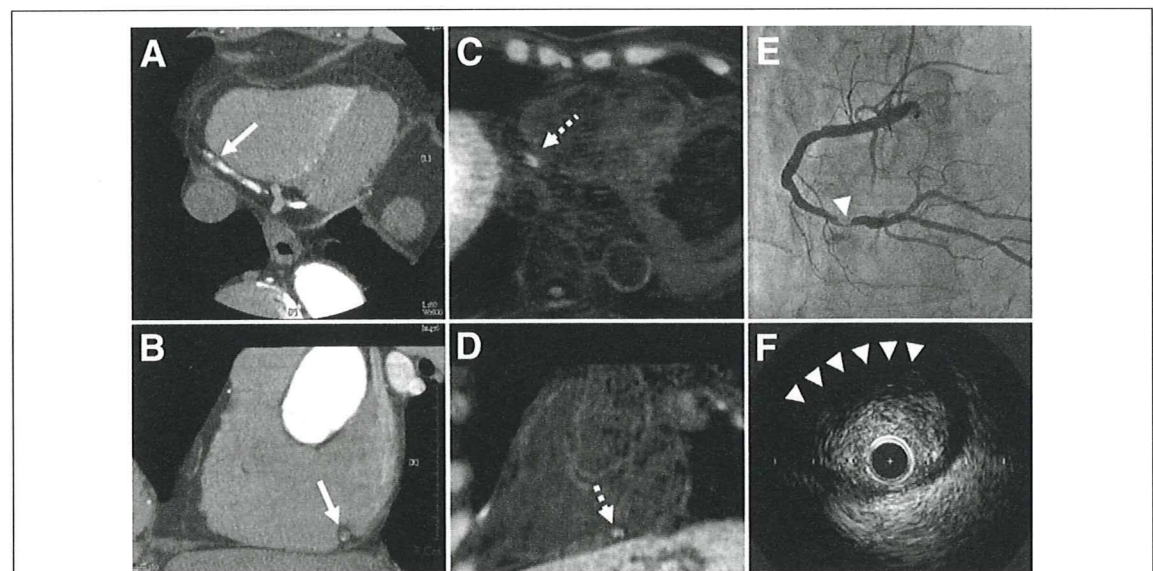

Figure 4. Representative Case of HIP in the Mid-RCA

A 60-year-old patient with a severe coronary stenosis in the mid-right coronary artery (RCA) is shown. Multislice computed tomography (MSCT) (**A:** horizontal, **B:** sagittal) shows the low-density positive remodeling plaque (–66 Hounsfield units, remodeling index: 1.15, **arrow**) with severe coronary stenosis in the mid-RCA. On the corresponding cardiac magnetic resonance (CMR) (**C:** horizontal, **D:** sagittal), a hyperintense plaque (HIP) can be observed by MSCT in the region with a low-density positive remodeling plaque (**dashed arrow**). On the coronary angiography, severe coronary stenosis was observed (**E**). On intravascular ultrasound examination (**F**), positive remodeling plaque (remodeling index: 1.13) with ultrasound attenuation (**white arrowheads**) was observed in the mid-RCA, corresponding with the plaque observed both by MSCT and CMR.

136

positive remodeling. These factors are recognized surrogate markers for vulnerable coronary plaques (14). Thus, the present findings—that in stable angina patients with HIP the rate of positive remodeling was high and similar to those for cases of acute coronary syndrome (15)—may be explained by the possibility that HIP may represent vulnerable coronary plaque. In other words, HIP itself may reflect positive remodeling, which represents a large volume of lipid content.

The mechanism of ultrasound attenuation is thought to involve the existence of microcalcification, thrombus, cholesterol crystals with expansive positive arterial remodeling (20,28), and large lipid-rich necrotic core (29,30). Furthermore, in histological IVUS examination, the necrotic core is significantly larger in plaques with ultrasound attenuation (20). On the other hand, it is well known that slow-flow/no-reflow phenomena may occur with high frequency during PCI treatment of ultrasound-attenuated plaques (18,28,29,31). In our study, transient slow-flow phenomena occurred in 15 (83%) of the 18 lesions with ultrasound attenuation in HIP, in contrast, only 1 (14%) of the 7 lesions without ultrasound attenuation in non-HIP behaved this way. Thus, HIP is thought to represent a great potential for high-risk plaque, which induces transient slow-flow phenomena during PCI.

Clinical impact of HIP on noncontrast T1W CMR. In the studies of the carotid artery using magnetic resonance imaging, HIP on T1WI has been reported with a histological correlation with methemoglobin in intraplaque hemorrhage (9,10). Because intraplaque hemorrhage is a criterion for complicated plaque (American Heart Association type VI) and patients with this type of carotid plaque exhibited ischemic cerebrovascular events and were therefore recognized as cases of vulnerable carotid plaque (10,11), noncontrast T1WI in CMR may enable noninvasive detection of advanced coronary plaque stages, such as carotid plaque. Based on carotid artery studies and our findings from MSCT and IVUS in this study, we speculate that the observed high signals in coronary plaque generated by noncontrast T1WI may represent intraplaque hemorrhage or lipid-rich necrotic cores and, therefore, may have potential as markers for plaque vulnerability.

Although the characterization of atherosclerotic plaque with a noninvasive imaging modality is still challenging, our findings detected by noncontrast T1WI may be informative findings to identify the plaque characteristics. Noninvasive, easily repeatable, and inexpensive methods that detect instability of coronary lesions are needed for the management of patients with high-risk coronary artery disease. In this regard, coronary plaque imaging using noncontrast T1WI may provide clinically important information regarding plaque vulnerability and clinical outcome. Further prospective studies are warranted to elucidate whether HIP has potential as a marker for vulnerability and clinical outcomes.

Study limitations. The number of subjects in this study was small. In addition, recruiting patients with significant coronary stenosis might have resulted in a certain bias, because IVUS examination is an invasive technique with associated non-negligible risks, and it is permitted only during PCI. Therefore, patients without significant coronary stenosis were excluded. However, IVUS is the current in vivo gold standard for coronary plaque assessment and is the only way to differentiate plaque characterization. Thus, we have chosen a group of selected patients with significant coronary stenosis. Because no comparison with histopathological data was performed in this study, precise characterization of HIP remains unknown. From the knowledge of carotid plaque evaluation using magnetic resonance imaging and pathological examination, the observed high signals generated by short T_1 plaques may represent intraplaque hemorrhage or necrotic lipid cores. These assumptions remain to be investigated in subsequent studies, and histological correlation is required for verification. Furthermore, only T1WI was used in this study. The time-of-flight image was considered to be a useful method for distinguishing intraplaque hemorrhage from lipid-rich necrotic cores (30). Another limitation of this study is that study patients presented with stable angina pectoris but not acute coronary syndrome; therefore, it remains unknown whether HIP detected by T1WI represents really vulnerable coronary plaques.

CONCLUSIONS

Hyperintense plaque on noncontrast T1WI is strongly associated with positive coronary remodeling, remarkably low CT density, and ultrasound attenuation. Thus, the data suggest that HIP detected by noncontrast T1WI may have potential for identifying vulnerable coronary lesions.

Reprint requests and correspondence: Dr. Tomohiro Kawasaki, Cardiovascular Center, Shin-Koga Hospital, 120, Tenjin-cho, Kurume 830-8577, Japan. *E-mail: tokawasaki@mug.biglobe.ne.jp.*

REFERENCES

1. Botnar RM, Stuber M, Kissinger KV, Kim WY, Spuentrup E, Manning WJ. Noninvasive coronary vessel wall and plaque imaging with magnetic resonance imaging. Circulation 2000; 102:2582–7.

2. Kim WY, Astrup AS, Stuber M, et al. Subclinical coronary and aortic atherosclerosis detected by magnetic resonance imaging in type 1 diabetes with and without diabetic nephropathy. Circulation 2007;115:228–35.

3. Kim WY, Stuber M, Bornert P, Kissinger KV, Manning WJ, Botnar RM. Three-dimensional black-blood cardiac magnetic resonance coronary vessel wall imaging detects positive arterial remodeling in patients with nonsignificant coronary artery disease. Circulation 2002;106:296–9.

4. Ferencik M, Nieman K, Achenbach S. Noncalcified and calcified coronary plaque detection by contrast-enhanced multi-detector computed tomography: a study of interobserver agreement. J Am Coll Cardiol 2006;47: 207–9.

5. Kopp AF, Schroeder S, Baumbach A, et al. Non-invasive characterisation of coronary lesion morphology and composition by multislice CT: first results in comparison with intracoronary ultrasound. Eur Radiol 2001;11:1607–11.

6. Ropers D, Baum U, Pohle K, et al. Detection of coronary artery stenoses with thin-slice multi-detector row spiral computed tomography and multiplanar reconstruction. Circulation 2003;107:664–6.

7. Schroeder S, Kopp AF, Baumbach A, et al. Noninvasive detection and evaluation of atherosclerotic coronary plaques with multislice computed tomography. J Am Coll Cardiol 2001; 37:1430–5.

8. Yeon SB, Sabir A, Clouse M, et al. Delayed-enhancement cardiovascular magnetic resonance coronary artery wall imaging: comparison with multislice computed tomography and quantitative coronary angiography. J Am Coll Cardiol 2007;50:441–7.

9. Moody AR, Murphy RE, Morgan PS, et al. Characterization of complicated carotid plaque with magnetic resonance direct thrombus imaging in patients with cerebral ischemia. Circulation 2003;107:3047–52.

10. Murphy RE, Moody AR, Morgan PS, et al. Prevalence of complicated carotid atheroma as detected by magnetic resonance direct thrombus imaging in patients with suspected carotid artery stenosis and previous acute cerebral ischemia. Circulation 2003;107: 3053–8.

11. Yamada N, Higashi M, Otsubo R, et al. Association between signal hyperintensity on T1-weighted MR imaging of carotid plaques and ipsilateral ischemic events. Am J Neuroradiol 2007;28:287–92.

12. Imazeki T, Sato Y, Inoue F, et al. Evaluation of coronary artery remodeling in patients with acute coronary syndrome and stable angina by multislice computed tomography. Circ J 2004;68:1045–50.

13. Ehara S, Kobayashi Y, Yoshiyama M, et al. Spotty calcification typifies the culprit plaque in patients with acute myocardial infarction: an intravascular ultrasound study. Circulation 2004; 110:3424–9.

14. Motoyama S, Kondo T, Sarai M, et al. Multislice computed tomographic characteristics of coronary lesions in acute coronary syndromes. J Am Coll Cardiol 2007;50:319–26.

15. Nakamura M, Nishikawa H, Mukai S, et al. Impact of coronary artery remodeling on clinical presentation of coronary artery disease: an intravascular ultrasound study. J Am Coll Cardiol 2001;37:63–9.

16. Schoenhagen P, Ziada KM, Kapadia SR, Crowe TD, Nissen SE, Tuzcu EM. Extent and direction of arterial remodeling in stable versus unstable coronary syndromes: an intravascular ultrasound study. Circulation 2000; 101:598–603.

17. Pasterkamp G, Borst C, Gussenhoven EJ, et al. Remodeling of de novo atherosclerotic lesions in femoral arteries: impact on mechanism of balloon angioplasty. J Am Coll Cardiol 1995;26:422–8.

18. Okura H, Taguchi H, Kubo T, et al. Atherosclerotic plaque with ultrasonic attenuation affects coronary reflow and infarct size in patients with acute coronary syndrome: an intravascular ultrasound study. Circ J 2007;71:648–53.

19. Maintz D, Ozgun M, Hoffmeier A, et al. Selective coronary artery plaque visualization and differentiation by contrast-enhanced inversion prepared MRI. Eur Heart J 2006;27:1732–6.

20. Yamada R, Okura H, Kume T, et al. Histological characteristics of plaque with ultrasonic attenuation: a comparison between intravascular ultrasound and histology. J Cardiol 2007;50: 223–8.

21. Motoyama S, Kondo T, Anno H, et al. Atherosclerotic plaque characterization by 0.5-mm-slice multislice computed tomographic imaging. Circ J 2007;71:363–6.

22. Glagov S, Weisenberg E, Zarins CK, Stankunavicius R, Kolettis GJ. Compensatory enlargement of human atherosclerotic coronary arteries. N Engl J Med 1987;316:1371–5.

23. Varnava AM, Mills PG, Davies MJ. Relationship between coronary artery remodeling and plaque vulnerability. Circulation 2002;105:939–43.

24. Fujii K, Carlier SG, Mintz GS, et al. Association of plaque characterization by intravascular ultrasound virtual histology and arterial remodeling. Am J Cardiol 2005;96:1476–83.

25. Higashikuni Y, Tanabe K, Yamamoto H, et al. Relationship between coronary artery remodeling and plaque composition in culprit lesions: an intravascular ultrasound radiofrequency analysis. Circ J 2007;71:654–60.

26. Okura H, Hayase M, Shimodozono S, Bonneau HN, Yock PG, Fitzgerald PJ. Impact of pre-interventional arterial remodeling on subsequent vessel behavior after balloon angioplasty: a serial intravascular ultrasound study. J Am Coll Cardiol 2001;38:2001–5.

27. Weissman NJ, Sheris SJ, Chari R, et al. Intravascular ultrasonic analysis of plaque characteristics associated with coronary artery remodeling. Am J Cardiol 1999;84:37–40.

28. Hara H, Tsunoda T, Moroi M, et al. Ultrasound attenuation behind coronary atheroma without calcification: mechanism revealed by autopsy. Acute Card Care 2006;8:110–2.

29. Furuichi S, Itoh A, Ishibashi-Ueda H, et al. Ultrasound attenuated coronary plaque as a risk factor for slow flow or no-reflow during percutaneous coronary intervention: a case report. J Cardiol 2007;49:193–7.

30. Yuan C, Mitsumori LM, Ferguson MS, et al. In vivo accuracy of multispectral magnetic resonance imaging for identifying lipid-rich necrotic cores and intraplaque hemorrhage in advanced human carotid plaques. Circulation 2001;104:2051–6.

31. Tanaka A, Kawarabayashi T, Nishibori Y, et al. No-reflow phenomenon and lesion morphology in patients with acute myocardial infarction. Circulation 2002;105:2148–52.

Key Words: coronary plaque imaging ▪ cardiac magnetic resonance ▪ multislice computed tomography ▪ intravascular ultrasound.

Characterization of Hyperintense Plaque With Noncontrast T1-Weighted Cardiac Magnetic Resonance Coronary Plaque Imaging: Comparison With Multislice Computed Tomography and Intravascular Ultrasound

Tomohiro Kawasaki, Shoichi Koga, Nobuhiko Koga, Teruo Noguchi, Hidenori Tanaka, Hisashi Koga, Takeshi Serikawa, Yoshiya Orita, Shinsuke Ikeda, Takahiro Mito, Yoshitaka Goto, Yoshiaki Shintani, Atsushi Tanaka, and Takaya Fukuyama

This information is current as of March 29, 2010

Updated Information & Services	including high-resolution figures, can be found at: http://imaging.onlinejacc.org/cgi/content/full/2/6/720
References	This article cites 31 articles, 21 of which you can access for free at: http://imaging.onlinejacc.org/cgi/content/full/2/6/720#BIBL
Citations	This article has been cited by 2 HighWire-hosted articles: http://imaging.onlinejacc.org/cgi/content/full/2/6/720#otherarticles
Rights & Permissions	Information about reproducing this article in parts (figures, tables) or in its entirety can be found online at: http://imaging.onlinejacc.org/misc/permissions.dtl
Reprints	Information about ordering reprints can be found online: http://imaging.onlinejacc.org/misc/reprints.dtl